Surface Science 640 (2015) 73–79

Contents lists available at ScienceDirect

Surface Science

journal homepage: www.elsevier.com/locate/susc

Structure of the $NiFe_2O_4(001)$ surface in contact with gaseous O_2 and water vapor

Xiao Shi, Ye-Fei Li [1], Steve L. Bernasek, Annabella Selloni *

Department of Chemistry, Princeton University, Princeton, NJ 08544, United States

ARTICLE INFO

Available online 24 March 2015

Keywords:
DFT calculations
Water adsorption
Oxygen vacancies

ABSTRACT

Nickel ferrite, $NiFe_2O_4$, is a material with interesting physical properties and useful technological applications. We have used Density-functional theory with on-site Coulomb repulsion U term to study the structure, electronic properties, and energetics of the $NiFe_2O_4(001)$ surface and its interaction with water both in the absence and in the presence of surface oxygen vacancies. In a humid environment, water adsorbs dissociatively on the surface oxygen vacancies leading to the formation of surface hydroxyls. At high temperature, water desorbs leaving a surface containing oxygen vacancies. These defects could represent useful reactive sites for various catalytic reactions.

1. Introduction

The spinel ferrites with general formula AFe_2O_4 are materials of both fundamental and technological interest [1]. In particular, $NiFe_2O_4$ is a promising material for magnetic storage systems [2], magnetic-resonance imaging [3], spintronics [4,5], etc. Recently, $NiFe_2O_4$ has also attracted significant attention for its catalytic activity for the oxygen evolution reaction [6], and as a potential catalyst for the Water Gas Shift (WGS) reaction [7], where the reactivity is limited by water desorption [8]. The interaction of $NiFe_2O_4$ surfaces with water plays a key role in all the applications of this material in catalysis. Understanding this interaction is thus essential for the design of more efficient $NiFe_2O_4$ catalysts for the WGS and other oxidation reactions.

While numerous theoretical [9] and experimental [10–12] investigations of the bulk electronic and magnetic properties of $NiFe_2O_4$ have been reported, studies on the surfaces of $NiFe_2O_4$ are still scarce. $NiFe_2O_4$ exposes different surfaces depending on the growth and preparation conditions [11,12], the (111) and (001) surfaces being the most frequent ones. For instance, hydrothermal synthesis of $NiFe_2O_4$ nanoparticles often leads to faceted octahedra enclosed by (111) planes [13], while films grown on $MgAl_2O_4$ or $SrTiO_3$ expose the (001) surface [11,12]. Recently, DFT calculations have shown that H_2O undergoes strong dissociative adsorption on the metal terminated (111) surface [13]. Instead, the structure of the (001) surface and its interaction with water have not yet been studied.

To help fill this gap, we present here a computational study of the structure of the $NiFe_2O_4(001)$ surface exposed to molecular oxygen and water vapor, the most common gases with which a surface can be in contact. Using the DFT + U method, we start by studying the electronic density of states (DOS) of bulk $NiFe_2O_4$ both in the absence and in the presence of an oxygen vacancy. These results are used as a reference in order to understand the effects of the (001) termination on the electronic structure. We next study the adsorption of water on both the defect-free and defected $NiFe_2O_4(001)$ surfaces. Our computed surface stability diagram predicts that the $NiFe_2O_4(001)$ surface is hydroxylated at ambient conditions, while it exhibits surface oxygen vacancies in the temperature range of 600–900 K that is often used for catalytic reactions.

2. Methods and models

DFT calculations were performed within the plane-wave–pseudopotential scheme as implemented in the Quantum Espresso package [14]. Spin polarization was always included, and exchange and correlation terms were described using the gradient corrected Perdew–Burke–Ernzerhof (PBE) [15] functional with the on-site Coulomb repulsion U term on the Fe and Ni 3 d states. We used the values U(Ni) = 5.5 eV and U(Fe) = 3.5 eV and 3.4 eV for different Fe sites, which were determined from linear response [16]. Ultrasoft pseudopotentials [17] were employed and the valence electrons included O 2 s, 2 p; Fe 3 d, 4 s and Ni 3 d, 4 s states. Kinetic energy cutoffs of 50 Ry and 500 Ry were chosen for the wave functions and augmented density, respectively. Structural optimizations were carried out by relaxing all atomic positions until all forces were smaller than 1×10^{-3} a.u.

Bulk calculations were performed using different unit cells. The lattice constant was determined using the 28-atom primitive cell (Fig. 1a), with a $4 \times 4 \times 3$ Monkhorst–Pack k-point grid to sample the Brillouin zone. To model a bulk oxygen vacancy, we used the

* Corresponding author.
[1] Present address: Department of Chemistry, Fudan University, Shanghai, Shanghai 200433, China.

http://dx.doi.org/10.1016/j.susc.2015.03.012
0039-6028/

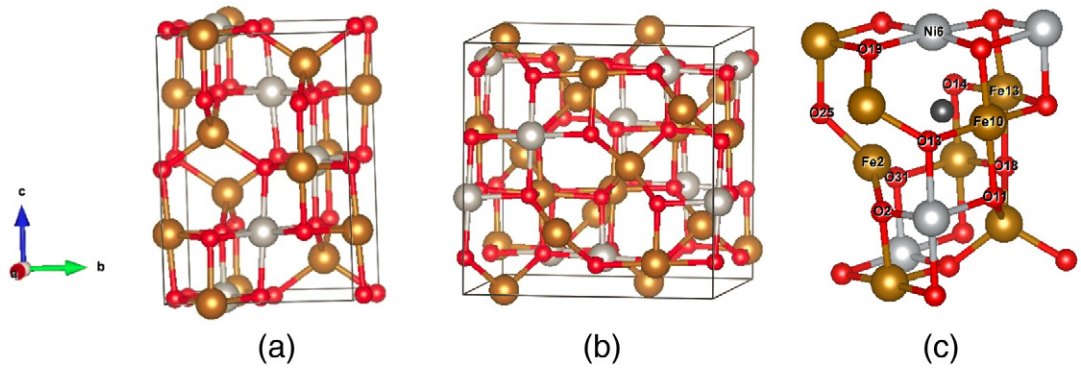

Fig. 1. Primitive cell (a), and conventional cell (b), of the α-type inverse spinel crystal structure of $NiFe_2O_4$. (c) Local structure of an oxygen vacancy (black sphere) in the conventional cell, with different atoms labeled as in Table 1. Red, gray and yellow spheres represent oxygen, Ni, and Fe atoms, respectively.

conventional cubic cell (Fig. 1b) with one oxygen atom removed, and sampled the Brillouin zone with a $3 \times 3 \times 3$ k-point grid.

As in previous studies of the surfaces of spinel oxides [18–20], we modeled the $NiFe_2O_4(001)$ surface using symmetric slabs of 11 layers terminated by layers exposing oxygen and octahedral Fe and Ni sites. The slabs were separated by a vacuum region 20 Å wide. To check the convergence of the slab thickness, we calculated the surface oxygen vacancy formation energy (see definition below) for slabs of different thicknesses; we found the formation energy difference between 11-layer and 13-layer slabs to be less than 0.01 eV. We considered 1×1 square unit cell, which corresponds to the conventional cell. We sampled the surface Brillouin zone using a $3 \times 3 \times 1$ k-point grid. Adsorption calculations and defected surface calculations were performed with adsorbed species and surface defects present on one side only of the slab (Model I). To validate this approach, we performed test calculations with adsorbed species and defects symmetrically present on both sides of the slab (Model II). We found that the two models predict very similar results. For instance, the computed surface oxygen vacancy formation energy at T = 0 K is 0.342 eV with Model I and 0.366 eV with Model II. Moreover, the value obtained for Model I changed by less than 0.01 eV when dipole corrections were included. Similarly, water dissociation at the surface vacancy yields an energy gain of 1.026 eV with Model I and 1.025 eV with Model II.

In order to study the surface phase diagram, we computed the formation energy $E_{F.E.}(T, \{p_i\}, \{n_i\})$ of the surface in contact with various gases at temperature T as follows: [21]

$$E_{F.E.}(T,\ \{p_i\},\{n_i\})\ =\ E_{tot}(\{n_i\}) - E_P - \sum_{gas} n_i\ \times\ u_i(T,p_i). \qquad (1)$$

Here, $\{p_i\}$ are the partial pressures of the gaseous species (oxygen and water), $\{n_i\}$ are the corresponding numbers of adsorbed/desorbed molecules on/from the surface, $E_{tot}(\{n_i\})$ is the total energy of the slab with the adsorbed/desorbed species at 0 K (the T-dependence of the chemical potential of the slab can be considered negligible), E_P is the total energy of the clean pristine (defect-free) surface, and $u_i(T, p_i)$ is the chemical potential of gas species i at temperature T and pressure p_i. For the latter, the expression given in Ref. [21] was used. The zero point energy (ZPE) contribution of molecular water and adsorbed water and hydroxide groups was included in the corresponding chemical potential and total energies.

As a special case of Eq. (1), the formation energy of an oxygen vacancy at 0 K and oxygen partial pressure of 1 atm was calculated using the expression $E_{FE} = E_{vac} - E_{no-def} - \frac{1}{2}E_{O_2}$, where E_{vac} and $E_{no\ -\ def}$ denote the total energies of the systems with and without vacancy, respectively.

3. Results and discussion

3.1. Bulk properties

$NiFe_2O_4$ crystallizes in the α type inverse spinel (Fig. 1a), which has a tetragonal $P4_122/P4_322$ symmetry [22]. Equal numbers of Ni and Fe atoms occupy octahedral sites, while the remaining Fe atoms occupy tetrahedral sites. The conventional cell (Fig. 1b) is a $\sqrt{2} \times \sqrt{2} \times 1$ primitive cell having 8 formula units. The lattice constant was determined by fitting the computed total energies to the Birch-Murnaghan equation of state. We obtained a value of 8.45 Å, which is about 1.4% larger than the experimental value of 8.33 Å [23].

The computed DOS for the defect-free crystal (Fig. 2a) shows an overall band gap of 1.0 eV. The band gap is 1.5 eV for the majority bands (spin-up) and 1.6 eV for the minority bands, in good agreement with the experimental value of the optical band gap of 1.6 eV [24]. Also in agreement with experiment [10,24], we find $NiFe_2O_4$ to be ferrimagnetic, the octahedral (Oh) and tetrahedral (Td) sites being occupied predominantly by majority and minority spins, respectively. The oxidation states of the metal ions, computed using the method in Ref. [25], are 2+ for Ni and 3+ for Fe.

As most oxidation reactions on metal oxides occur through a Mars–Van Krevelen mechanism, the oxygen vacancy formation energy is usually considered a good descriptor of the reactivity of these materials [26]. $NiFe_2O_4$ contains two inequivalent oxygen anions: O_I, bound to 2 Fe and 1 Ni at Oh sites and 1 Fe at Td, and O_{II}, bound to 1 Fe and 2 Ni at Oh sites and 1 Fe at Td. We found that an O_I vacancy is slightly preferred (less costly) with respect to an O_{II} one. Still, the computed formation energy, 2.87 eV, is rather high indicating that one may need high vacuum and high temperatures to create oxygen vacancies in bulk $NiFe_2O_4$. For comparison, we also computed the oxygen vacancy formation energy in Co_3O_4, another well-studied spinel oxide, using DFT + U with U = 4.4 and 6.6 eV for Co ions at Td and Oh sites, respectively [27]. The resulting value, 2.88 eV, is very similar to that found for $NiFe_2O_4$.

The displacements of several atoms around the oxygen vacancy are reported in Table 1. Fe_2, the Fe(Td) cation closest to the oxygen vacancy (which was originally bonded to the removed O atom), undergoes a large displacement, 0.46 Å, with respect to its position in the defect-free crystal. Large displacements of about 0.1 Å are present also for a few oxygens (O_2, O_{25} and O_{31}) bonded to Fe_2. The electronic DOS for the defective crystal is shown in Fig. 2b. We can see that the DOS for the majority spin states is little affected by the O-vacancy, whereas additional bands are present for the minority spin states, in particular a new occupied state above the original minority band valence band maximum. This results in a smaller minority band gap of ~1.0 eV. At the same time, the Fermi levels moves up in the band gap consistent with the fact that the O-vacancy is an electron donor. Analysis of the spin

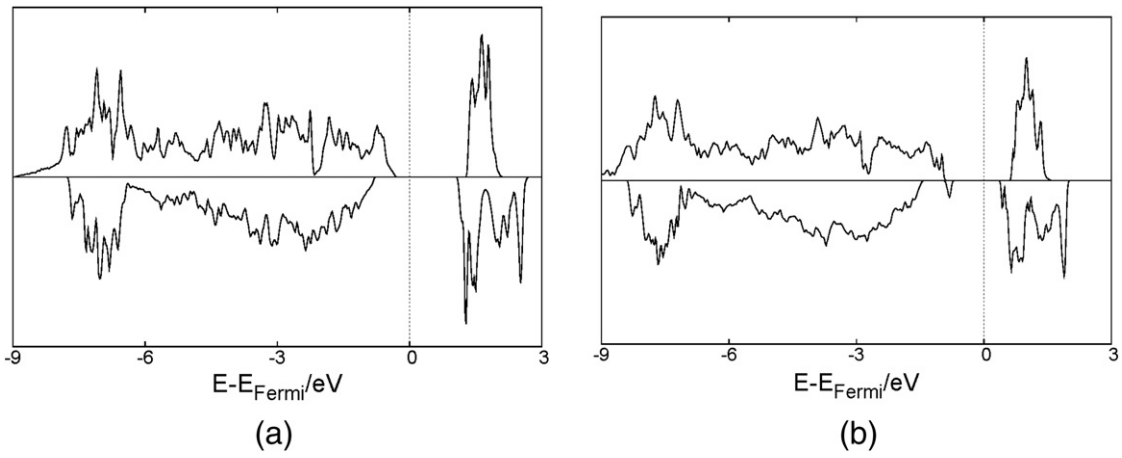

Fig. 2. Density of states for: (a) defect-free bulk $NiFe_2O_4$; (b) defective crystal with an oxygen vacancy (Fig. 1c).

and charge distribution further shows that one of the two excess electrons donated by the O-vacancy reduces the oxidation state of the neighboring Fe_2(Td) cation from 3+ to 2+, and at the same time reduces also its magnetic moment. The other excess electron is shared by the three neighboring Fe_{10}, Fe_{13} and Ni_6 cations at Oh sites and slightly reduces their magnetic moments. Since Td and Oh sites have different spin states, the total magnetization remains unchanged in the presence of the O-vacancy.

3.2. $NiFe_2O_4$(001) surface

3.2.1. Defect-free surface

The optimized structure of the $NiFe_2O_4$(001) surface is shown in Fig. 3, while the atomic displacements relative to the positions of the bulk-terminated surface are reported in Table 2. We can see significant outward displacements of the atoms in the first three layers in comparison to the positions of the bulk-terminated surface. Particularly large (>0.1 Å) displacements along the [001] direction are present for Fe_2(Td) in the second layer, and for O_2, O_3, O_4 in the top three layers. Large in plane displacements are also present for O_2 and O_3, the surface oxygens that are not bonded to Fe_2.

The DOS (Fig. 4a) for the defect-free $NiFe_2O_4$(001) surface shows the formation of surface states in the band gap of the majority spin DOS which make the surface metallic. An analogous result was found for the Co_3O_4(110) surface [18]. By contrast, the minority spin band is almost unaffected by the presence of the surface and remains very similar to the minority spin band in the bulk. The computed work function was determined from the analysis of the electrostatic potential profile, and found to have a value of about 6 eV.

3.2.2. Surface O vacancy

To determine the preferred structure of $NiFe_2O_4$(001), we studied the formation of 1 and 2 surface oxygen vacancies (V_O's) per unit cell, corresponding to surface V_O concentrations of 1/8 (Fig. 5a) and 1/4 (Fig. 5b), respectively. The formation of 1 V_O/unit cell has an energy cost of 0.34 eV at 0 K and 1 atm O_2 pressure. The most favorable site for V_O formation is the O_3 site, i.e. the oxygen that bonds to two Ni cations (Ni_1 and Ni_2) and one Fe (Fe_1). By comparing to the bulk formation energy of 2.87 eV, it is clear that creating an oxygen vacancy at the surface is much easier than in the bulk. This remains true also at higher V_O concentrations, even though the V_O formation energy increases significantly with increasing concentration. The formation of 2 oxygen vacancies per unit cell (Fig. 5b) has indeed an energy cost of 1.43 eV, which corresponds to an average formation energy of 0.71 eV per vacancy. The two oxygen vacancies prefer to form both at O3 sites, and all O3 anions are removed by forming 2 oxygen vacancies/unit cell. Formation of the second oxygen vacancy at O2, which binds to 2 Fe(Oh) site and 1 Ni(Oh), has a slightly higher energy cost than at the O_3 site, whereas O_1 is much harder to remove. Since O_1 binds to Fe_2(Td), removing O_1 would indeed result in a undercoordinated Fe(Td) which is much more unstable.

The DOS for the surface with 1/8 V_O coverage is shown in Fig. 4b. We can see a change in the majority spin surface state band, which results in the opening of a narrow band gap of ~0.1 eV at the Fermi level. On the other hand, the minority spin band does not change significantly except for a small increase, by 0.1 eV, of the band gap. The computed work function, 5.9 eV, remains almost unchanged relative to the one for the pristine surface.

Table 1
Displacements of the atoms close to a bulk O-vacancy (Fig. 1c) with respect to their positions in the defect-free crystal (Fig. 1b). Atoms are labeled as in Fig. 1c. Only the atoms closest to the vacancy are considered.

	Displacement (Å)		
	x	y	z
O_2	0.071	−0.044	−0.048
O_{11}	0.008	0.044	0.045
O_{13}	−0.041	0.005	0.053
O_{14}	0.051	0.012	−0.047
O_{18}	0.057	0.054	−0.001
O_{19}	−0.033	−0.011	−0.004
O_{25}	0.077	0.055	0.075
O_{31}	−0.025	−0.052	0.056
Fe_2	0.281	−0.242	0.273
Fe_{10}	−0.029	0.021	−0.009
Fe_{13}	−0.036	0.021	−0.033
Ni_6	−0.010	0.060	−0.017

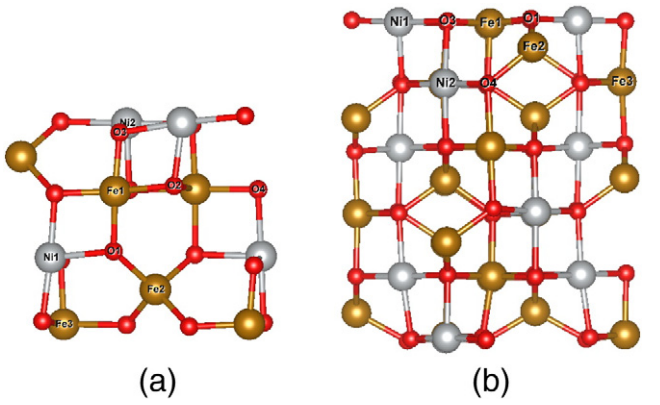

Fig. 3. Structure of the $NiFe_2O_4$(001) surface: (a) top view of the top three layers, and (b) side view. Various O, Fe and Ni atoms are indicated.

Table 2
Displacements of the atoms in the first three layers of the relaxed (001) surface relative to their positions at the bulk-terminated surface.

Displacements Å	In plane	(001) direction
O_1	0.098	0.026
O_2	0.185	0.126
O_3	0.185	0.080
O_4	0.085	0.108
Ni_1	0.026	0.024
Ni_2	0.017	0.062
Fe_1	0.049	0.036
Fe_2	0.042	0.196
Fe_3	0.062	0.082

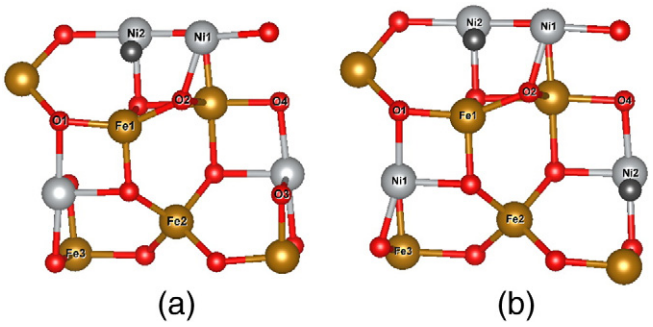

Fig. 5. Top views of the first three layers of the $NiFe_2O_4(001)$ surface in the presence of (a) 1 O-vacancy ($P + 1V_O$) (b) 2 O-vacancies ($P + 2V_O$). The oxygen vacancies are indicated by the black spheres. Atoms are labeled as in Fig. 3.

3.3. Water adsorption

3.3.1. Water adsorption on the defect-free surface

The adsorption structures of water on the pristine $NiFe_2O_4(001)$ surface are found to vary significantly with coverage. At 1/4 monolayer (ML) coverage, corresponding to 1 water molecule per surface cell (Fig. 5a), water adsorbs in molecular form on a Ni cation, whereas it dissociates on Fe, resulting in an OH on top of the Fe ion and an H donated to a surface oxygen. The adsorption energy on Ni is 0.53 eV, which is about 0.1 eV more favorable to that on Fe. At 1/2 ML coverage (Fig. 5b), the two water molecules prefer to adsorb both in molecular form, one on a Ni site and one on a Fe site, with an adsorption energy of 0.44 eV/H_2O. At 3/4 ML coverage (Fig. 5c), the most stable configuration corresponds to two water molecules adsorbed in molecular form on Ni sites and one dissociated water on a Fe site, and the adsorption energy is 0.58 eV/H_2O. Finally, the preferred configuration at full water coverage has all the 4 water molecules adsorbed in molecular form (Fig. 5d): two on Ni, one on Fe and one forming an H-bond with an O site, with average adsorption energy of 0.52 eV/H_2O. A mixed molecular-dissociated structure with two intact and two dissociated water molecules adsorbed on Ni and Fe sites, respectively, was found to be slightly higher in energy.

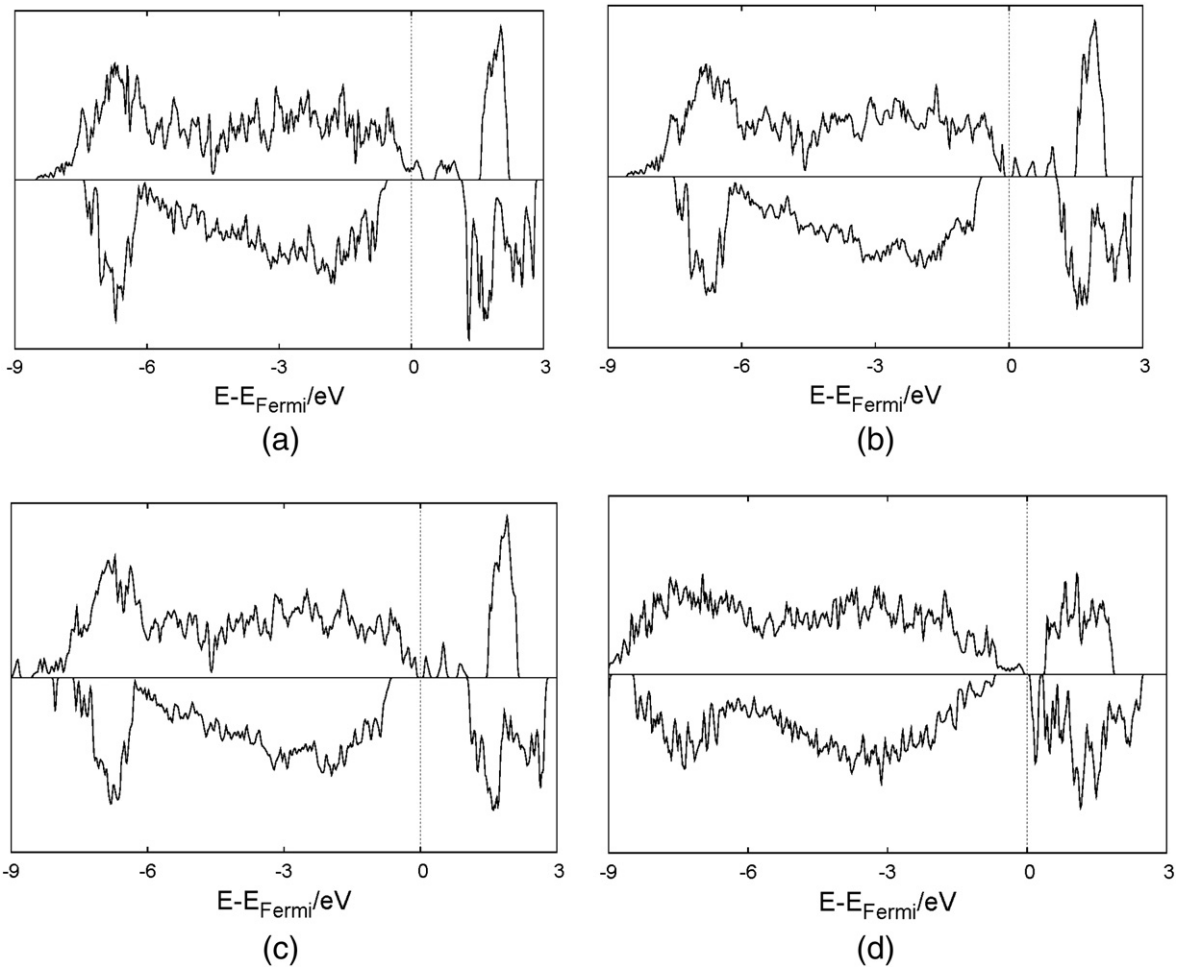

Fig. 4. DOS for: (a) clean defect-free $NiFe_2O_4(001)$ (denoted as P); (b) clean surface with 1 oxygen vacancy/unit cell ($P + 1V_O$); (c) hydroxylated surface resulting from the adsorption of 1 water molecule/unit cell on the surface in (b) ($P + 1V_O + 1H_2O$); (d) fully water-covered surface resulting from the adsorption of 6 water molecules/unit cell on the surface with 25% concentration of oxygen vacancies ($P + 2V_O + 6H_2O$).

The phase diagram for the pristine surface exposed to water is shown in Fig. 6. This was obtained by considering the dependence of the computed surface formation energies on the water chemical potential $\Delta u_{H_2O}(T, p_{H_2O}) = u_{H_2O}(T, p_{H_2O}) - E_{H_2O}$, where E_{H_2O} denotes the total energy (including ZPE) of a water molecule at T = 0 K. This diagram predicts that all water desorbs from the pristine surface at temperatures above ~300 K.

3.3.2. Water adsorption on the defected surface

Fig. 7 shows some adsorption structures of water on defected $NiFe_2O_4(001)$ surfaces at various coverages. From the reported adsorption energies (Eads), we can see that water adsorption is much more favorable on the defected surface than on the pristine surface (Fig. 6). In the presence of a surface oxygen vacancy (Fig. 5a, structure P + 1Vo), a water molecule dissociates on the V_O giving rise to two surface hydroxyls with Eads = 0.90 eV (Fig. 7a, structure P + 1Vo + $1H_2O$). By adsorbing three additional water molecules to this structure, the water molecule adsorbed on the Fe site dissociates into OH groups while the other two molecules at Ni sites remain intact (Fig. 7b, P + 1Vo + $4H_2O$). The average adsorption energy per molecule is 0.70 eV, which is smaller than the value for a single water molecule in Fig. 7a. On the surface with two oxygen vacancies (P + 2Vo), the configuration with two water molecules adsorbed dissociatively on the two V_O's gives the highest adsorption energy, 1.23 eV/molecule (structure P + 2Vo + $2H_2O$, Fig. 7c). When two additional water molecules are adsorbed on this surface, one prefers to adsorb in molecular form on a Ni site, while the other is dissociatively adsorbed on a Fe site (Fig. 7d, P + 2Vo + $4H_2O$). The adsorption energy, 0.86 eV/molecule, is lower compared to Fig. 7c but still quite higher than water adsorbed on the pristine surface. Finally, the addition of two further water molecules leads to a configuration where all metal sites are covered by adsorbed water (Fig. 7e, P + 2Vo + $6H_2O$). The two added molecules dissociate on Fe_1 sites and the average adsorption energy is 0.72 eV/molecule. Altogether, it appears that mixed molecular-dissociated configurations are favored at high coverages. Water dissociation takes place both at oxygen vacancies and at Fe sites, whereas adsorption in molecular form is preferred at Ni sites.

The DOS for the surface with an adsorbed water molecule at an oxygen vacancy site (Fig. 4c) is very similar to that of the bare surface with the V_O (Fig. 4b). Analysis of the surface metal oxidation states shows that also these oxidation states remain unchanged upon water adsorption. Altogether, this indicates that the influence of adsorbed water on the surface electronic structure is rather limited. Support for this conclusion is also provided by the DOS for the fully hydrated surface (Fig. 7e), which is shown in Fig. 4d. Comparison to the DOS in Fig. 4b and c for the clean defective and hydroxylated surfaces indicates that the main effect of the adsorbed water is the presence of additional bands for both spin states in the band gap near the Fermi level.

3.4. Phase diagram

In order to characterize the stability of the (001) surface in O_2 and water vapor environment, we examined about 30 surface configurations without and with adsorbed water and used them to determine the stability diagram of the $NiFe_2O_4(001)$ surface in O_2 and water vapor environment. The resulting diagram is shown in Fig. 8. We identified eight favored structures in the relevant range of water and oxygen chemical potentials. Among these, two structures, i.e. P + $1V_O$ and P + $2V_O$ + $2H_2O$, are more prominent. In a wide range of conditions including ambient conditions, the P + $2V_O$ + $2H_2O$ structure, corresponding to a surface with ~25% of hydroxyls, is predicted to occur. At higher temperatures, water desorbs and a dry surface with oxygen vacancies (~12% concentration) becomes more favorable. The latter structure may be the one which is typically present during catalytic reactions like the WGS and the CO oxidation reactions.

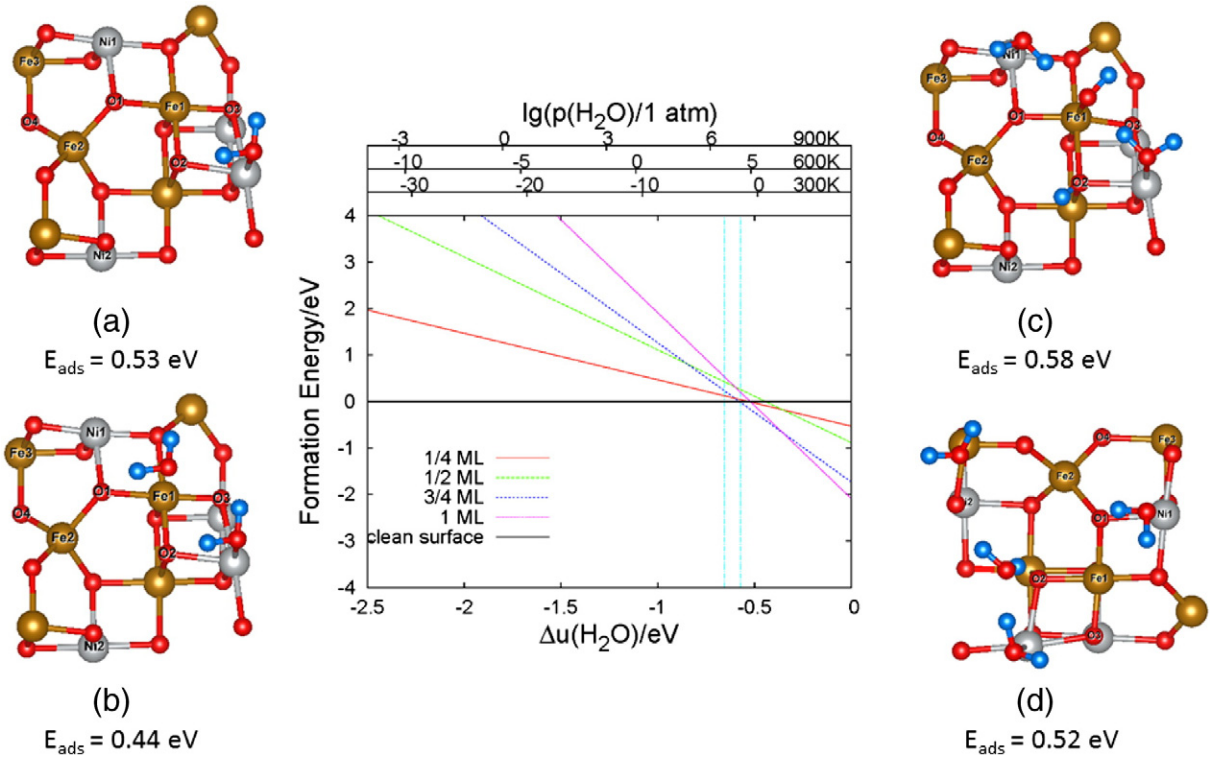

Fig. 6. Phase diagram of pristine $NiFe_2O_4(001)$ exposed to water vapor. The two vertical lines in cyan indicate the region of water chemical potential corresponding to liquid water (300 K–400 K). The side panels show the structures of adsorbed water at different coverages (top views). (a) 1/4 ML, (b) 1/2 ML, (c) 3/4 ML, (d) 1 ML. Reported adsorption energies include the change of zero point energies.

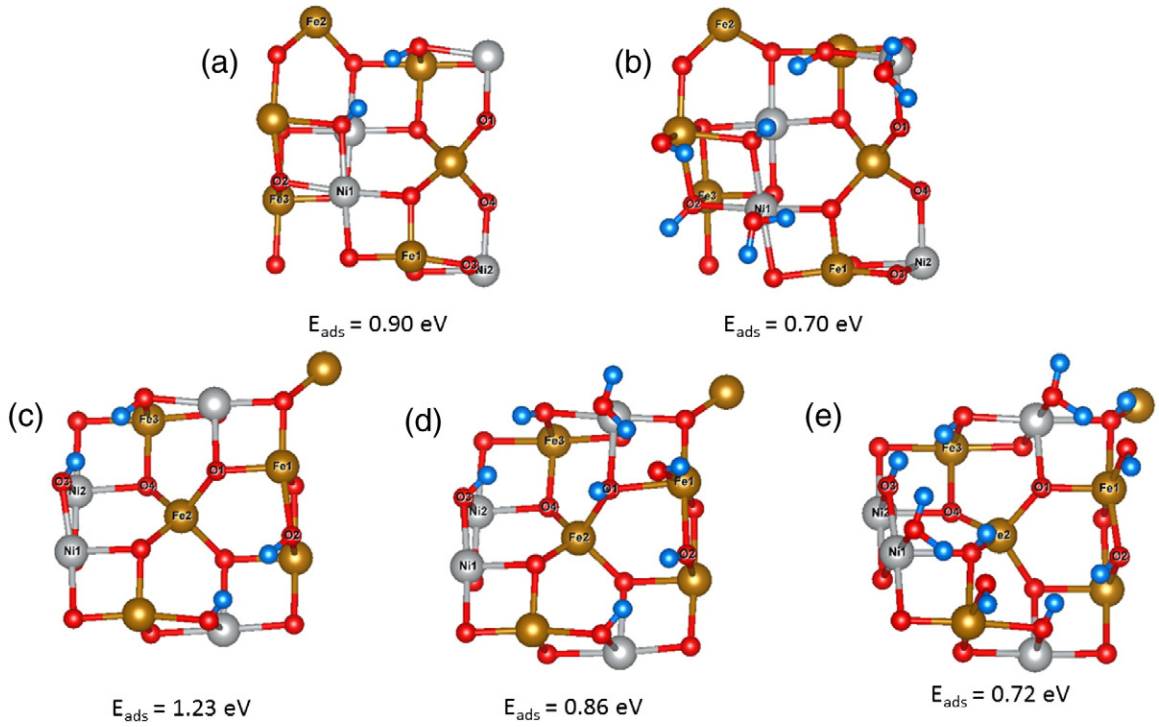

Fig. 7. Adsorption structures (top views) of water on defected $NiFe_2O_4$(001) surfaces at different coverages: (a) one water molecule adsorbed to a surface with 1 oxygen vacancy ($P + 1V_O + 1H_2O$), (b) four water molecules adsorbed to a surface containing 1 oxygen vacancy ($P + 1V_O + 4H_2O$), (c) two water molecules adsorbed to two oxygen vacancies ($P + 2V_O + 2H_2O$), (d) four water molecules adsorbed to a surface containing 2 oxygen vacancies ($P + 2V_O + 4H_2O$), (e) six water molecules adsorbed to a surface with two oxygen vacancies ($P + 2V_O + 6H_2O$). All structures shown refer to a single surface cell. Reported adsorption energies per molecule include ZPE corrections.

4. Summary and conclusions

We have studied the atomic structure, electronic properties, and reactivity of the bulk and (001) surface of $NiFe_2O_4$ using the PBE + U method. Our results show that, unlike in the bulk, oxygen vacancies form quite easily on the nickel ferrite surface, especially at oxygen sites that are coordinated mainly to Ni ions. Our results also indicate that dissociative adsorption of water at vacancy sites is much more favorable than adsorption at regular surface sites thus suggesting that a humid environment may help the creation of oxygen vacancies. From our computed surface phase diagram we infer that the $NiFe_2O_4$(001) is hydroxylated at ambient conditions, while water desorption should lead to a defective surface containing a significant fraction of oxygen vacancies at higher temperature.

It is also interesting to notice that our computed phase diagram for $NiFe_2O_4$(001) in Fig. 8 is significantly different from that for the Fe_3O_4 (001) surface [28] exposed to water and oxygen, despite the similarity of the two surfaces. In comparison to $NiFe_2O_4$(001), the Fe_3O_4 (001) surface shows a stronger tendency to adsorb water whereas formation of an oxygen vacancy appears to be much more difficult. Due to its tendency to easily form surface oxygen vacancies, the $NiFe_2O_4$(001) surface should be a promising catalyst material for oxidation reactions occurring through the Mars–Van Krevelen mechanism.

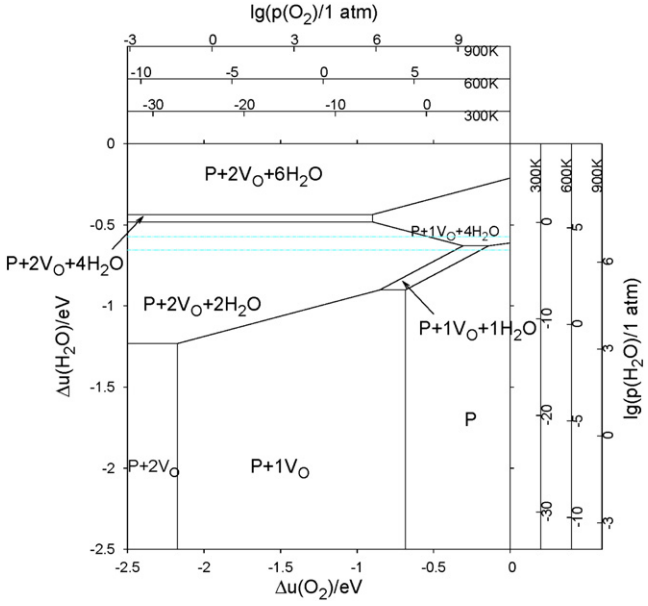

Fig. 8. Phase diagram of $NiFe_2O_4$(001) exposed to H_2O and O_2, as a function of the relative chemical potentials $\Delta u_i(T, p_i) = u_i(T, p_i) - E_i$ referred to the their values at T = 0 K. The two horizontal lines in cyan indicate the region of water chemical potential corresponding to liquid water. P in the phase diagram indicates the pristine (001) surface.

Acknowledgments

This work was supported by DoE–BES, Division of Chemical Sciences, Geosciences and Biosciences under Award DE-FG02-12ER16286. SLB acknowledges support from NSF CHE1213216. We used resources of the National Energy Research Scientific Computing Center (DoE Contract No. DE-AC02-05CH11231), and of the Center for Functional Nanomaterials at Brookhaven National Laboratory. We also acknowledge the use of the TIGRESS high performance computer center at Princeton University.

References

[1] V.A.M. Brabers, Chapter 3 progress in spinel ferrite, research, 81995. 189.
[2] D.-H. Han, H.-L. Luo, Z. Yang, J. Magn. Magn. Mater. 161 (1996) 376.
[3] C.H. Cunningham, T. Arai, P.C. Yang, M.V. McConnell, J.M. Pauly, S.M. Conolly, Magn. Reson. Med. 53 (2005) 999.
[4] D.C. Worledge, T.H. Geballe, J. Appl. Phys. 88 (2000) 5277.
[5] G. Hu, Y. Suzuki, Phys. Rev. Lett. 89 (2002).
[6] D. Hong, Y. Yamada, T. Nagatomi, Y. Takai, S. Fukuzumi, J. Am. Chem. Soc. 134 (2012) 19572.

[7] G.K. Reddy, K. Gunasekera, P. Boolchand, J. Dong, P.G. Smirniotis, J. Phys. Chem. C 115 (2011) 7586.
[8] C. Zhou, Q. Zhang, L. Chen, B. Han, G. Ni, J. Wu, D. Garg, H. Cheng, J. Phys. Chem. C 114 (2010) 21405.
[9] Q.-C. Sun, H. Sims, D. Mazumdar, J.X. Ma, B.S. Holinsworth, K.R. O'Neal, G. Kim, W.H. Butler, A. Gupta, J.L. Musfeldt, Phys. Rev. B 86 (2012).
[10] V. Šepelák, D. Baabe, D. Mienert, D. Schultze, F. Krumeich, F.J. Litterst, K.D. Becker, J. Magn. Magn. Mater. 257 (2003) 377.
[11] U. Luders, M. Bibes, J.F. Bobo, J. Fontcuberta, Appl. Phys. A 80 (2004) 427.
[12] C. Klewe, M. Meinert, A. Boehnke, K. Kuepper, E. Arenholz, A. Gupta, J.M. Schmalhorst, T. Kuschel, G. Reiss, J. Appl. Phys. 115 (2014) 123903.
[13] P.V. Kumar, M.P. Short, S. Yip, B. Yildiz, J.C. Grossman, J. Phys. Chem. C 117 (2013) 5678.
[14] P. Giannozzi, S. Baroni, N. Bonini, M. Calandra, R. Car, C. Cavazzoni, D. Ceresoli, G.L. Chiarotti, M. Cococcioni, I. Dabo, A. Dal Corso, S. de Gironcoli, S. Fabris, G. Fratesi, R. Gebauer, U. Gerstmann, C. Gougoussis, A. Kokalj, M. Lazzeri, L. Martin-Samos, N. Marzari, F. Mauri, R. Mazzarello, S. Paolini, A. Pasquarello, L. Paulatto, C. Sbraccia, S. Scandolo, G. Sclauzero, A.P. Seitsonen, A. Smogunov, P. Umari, R.M. Wentzcovitch, J. Phys. Condens. Matter 21 (2009).
[15] J.P. Perdew, K. Burke, M. Ernzerhof, Phys. Rev. Lett. 77 (1996) 3865.
[16] M. Cococcioni, S. de Gironcoli, Phys. Rev. B 71 (2005).
[17] D. Vanderbilt, Phys. Rev. B 41 (1990) 7892.
[18] J. Chen, A. Selloni, Phys. Rev. B 85 (2012) 085306.
[19] N. Mulakaluri, R. Pentcheva, M. Scheffler, J. Phys. Chem. C 114 (2010) 11148.
[20] N. Mulakaluri, R. Pentcheva, M. Wieland, W. Moritz, M. Scheffler, Phys. Rev. Lett. 103 (2009) 176102.
[21] K. Reuter, M. Scheffler, Phys. Rev. B 68 (2003) 045407.
[22] V.G. Ivanov, M.V. Abrashev, M.N. Iliev, M.M. Gospodinov, J. Meen, M.I. Aroyo, Phys. Rev. B 82 (2010).
[23] O. Madelung, U. Rössler, M. Schulz, Springer Mater. 26 (1991) 2621.
[24] H. Perron, T. Mellier, C. Domain, J. Roques, E. Simoni, R. Drot, H. Catalette, J. Phys. Condens. Matter 19 (2007) 346219.
[25] P.H.L. Sit, R. Car, M.H. Cohen, A. Selloni, Inorg. Chem. 50 (2011) 10259.
[26] E.W. McFarland, H. Metiu, Chem. Rev. 113 (2013) 4391.
[27] J. Chen, X. Wu, A. Selloni, Phys. Rev. B 83 (2011) 245204.
[28] N. Mulakaluri, R. Pentcheva, M. Wieland, W. Moritz, M. Scheffler, Phys. Rev. Lett. 103 (2009).